A&A 431, 979–991 (2005)
DOI: 10.1051/0004-6361:20041482

Astronomy & Astrophysics

The disrupted molecular envelope of Frosty Leo⋆,⋆⋆

A. Castro-Carrizo[1], V. Bujarrabal[2], C. Sánchez Contreras[3,4], R. Sahai[4], and J. Alcolea[5]

[1] Institut de RadioAstronomie Millimétrique, 300 rue de la Piscine, 38406 Saint Martin d'Hères, France
e-mail: ccarrizo@iram.fr
[2] Observatorio Astronómico Nacional (IGN), Apdo. 112, 28803 Alcalá de Henares, Spain
e-mail: v.bujarrabal@oan.es
[3] Caltech Astronomy Department, MS 105-24, California Institute of Technology, Pasadena, CA 91125, USA
e-mail: sanchez@astro.caltech.edu
[4] Jet Propulsion Laboratory, MS 183-900, California Institute of Technology, Pasadena, CA 91109, USA
e-mail: Raghvendra.Sahai@jpl.nasa.gov
[5] Observatorio Astronómico Nacional (IGN), c/ Alfonso XII 3, 28014, Madrid, Spain
e-mail: j.alcolea@oan.es

Received 17 June 2004 / Accepted 19 October 2004

Abstract. We present maps of CO emission in the protoplanetary nebula Frosty Leo. Observations of the rotational transitions ^{12}CO $J = 2-1$ and 1–0 have been obtained with the IRAM interferometer and the OVRO array. The molecular envelope of Frosty Leo is found to be complex and compact; most of the gas extends $\lesssim 6''$ and shows a structure that is very different to the extended optical nebula. It is composed of a central ring-like structure, whose symmetry axis is inclined $\sim -40°$ with respect to the sky plane and expands at speeds of up to $\sim$30 km s^{-1}, and high-velocity jets distributed along the symmetry axis of the ring, which reach expansion velocities as high as $\sim$75 km s^{-1}. The symmetry axis of the molecular jets in the plane of the sky coincides with the direction of some jet-like features seen in the optical, which are not aligned at all with the main symmetry axis of the optical nebula. The brightness distribution of the ring presents a clumpy structure. We have modeled the spatio-kinematical distribution of, and the excitation conditions in, the molecular envelope. For both transitions, the ^{12}CO emission is found to be very optically thick in the center of the nebula. From our best-fit model, we find that the nebular particle density varies between $\sim 10^5$ cm^{-3} and $\sim 10^3$ cm^{-3}, and that the rotational temperature is very low, $\sim$10 K. The kinematical lifetime of the molecular jets is $\sim$1700 yr, long in comparison with the lifetime of the post-AGB winds of most PPNe. It is very remarkable that the bulk of the gas accelerated during the post-AGB phase of Frosty Leo is located within the central ring, reaching expansion velocities of up to $\sim$30 km s^{-1}. The central ring-like distribution of Frosty Leo is probably not the undisrupted remnant of the previous AGB envelope (as found for most PPNe), but its dynamics likely result from multiple post-AGB interactions.

Key words. stars: individual: Frosty Leo – stars: circumstellar matter – stars: AGB and post-AGB – radio lines: stars – stars: mass-loss

1. Introduction

Once stars leave the asymptotic giant branch (AGB), the circumstellar envelopes formed around them evolve into planetary nebulae (PNe) in just a few thousand years, the protoplanetary nebulae (PPNe) being the intermediate stage.

In 1987, Forveille et al. identified Frosty Leo (IRAS 09371+1212) as a PPN, from the analysis of its CO emission and its visible spectrum. The spectral type of its central star is K7III, i.e. its effective temperature is $\sim$3700 K (Mauron et al. 1989; Robinson et al. 1992). Its bolometric luminosity is $\sim 250\ D^2\ L_\odot$ (Forveille et al. 1987), where D is the distance (in kpc) which has been estimated to range between 1 and 4 kpc (Mauron et al. 1989). According to its post-AGB nature, Robinson et al. (1992) argue that its bolometric luminosity should be $\gtrsim$1500 $L_\odot$, i.e. its distance $\gtrsim$2.5 kpc, while Phillips & Cuesta (1997) and Langill et al. (1994) suggest that the luminosity should be >3000 $L_\odot$, that is $D > 3.5$ kpc. It is usually assumed that $D \sim 3$ kpc (e.g. Sahai et al. 2000), and so we have adopted this value for most of our work. However, given its uncertainty we will briefly analyze the case of the most extreme distances discussed by Mauron et al. (1989) in Sect. 6.

Images in the optical and near infrared show an extended nebula, with a remarkable bipolar symmetry. The tips of the

⋆ Based on observations carried out with the IRAM Plateau de Bure Interferometer and with the OVRO Interferometer. IRAM is supported by INSU/CNRS (France), MPG (Germany) and IGN (Spain).
⋆⋆ Figures 1, 5 and 9 are only available in electronic form at http://www.edpsciences.org

lobes are bright, and at the nebula center the presence of a disk almost edge-on is inferred (see Morris & Reipurth 1990; Langill et al. 1994 and Sahai et al. 2000). Mauron et al. (1989) found that the optical light coming from Frosty Leo is highly polarized, suggesting that it is scattered by dust grains. No detection of emission lines due to shocked gas has been reported in the optical or in the near infrared (Morris & Reipurth 1990). The high-resolution optical image obtained by Sahai et al. (2000; see Fig. 1 in the electronic version), with the Hubble Space Telescope, also shows the presence of several jets relatively close to the equatorial plane. Additional multiple and complex substructures, detected in this image, suggest that the direction and momentum of the jets might have changed with time. The position angle (PA, from north to east on the plane of the sky) of the (main) symmetry axis of the optical nebula is ∼150°, and its inclination (Lopez et al. 2001) with respect to the plane of the sky is ∼16°, the south lobe being closer to us. Dougados et al. (1992), Scarrott & Scarrott (1994) and Phillips & Cuesta (1997) studied in detail the nature and the kinematics of dust. The mass estimated for the dust is $\sim[10^{-3}-10^{-4}]\ D^2\ M_{\odot}$.

Sahai et al. (2000) and Bujarrabal et al. (2001) analyze single-dish, high-sensitivity observations of the rotational transitions $J = 2-1$ and $J = 1-0$ of ^{12}CO and ^{13}CO in Frosty Leo. They estimate the mass, linear momentum and kinetic energy of the different components identified in the molecular line profiles. The very large amount of mass accelerated in the post-AGB phase in Frosty Leo is noteworthy; this PPN has the highest amount of linear momentum (P) and kinetic energy measured so far in the accelerated winds of PPNe. Note that, although these dynamical parameters depend on the distance, their ratio with the momentum of the stellar luminosity per unit of time (L/c) does not. The value of this momentum ratio for the accelerated winds in Frosty Leo, $\frac{P}{L/c} \sim 2 \times 10^5$, is one of the highest figures obtained in a PPN, only comparable to that estimated for CRL 618 (see Bujarrabal et al. 2001 and Sánchez Contreras et al. 2004).

In this paper, we present maps with high spatial resolution and sensitivity of the emission of ^{12}CO $J = 2-1$ and ^{12}CO $J = 1-0$ from Frosty Leo. These maps were obtained with the Plateau de Bure interferometer (France) and the OVRO array (USA). High velocity outflows have been detected, although most of the gas accelerated in the post-AGB phase remains within a ring-like compact structure. These high-velocity molecular outflows appear to be the molecular counterparts of remarkable jet-like features seen in the optical image by Sahai et al. (2000). The complex structure and dynamics of this nebula have been studied in detail.

2. Interferometric observations and data reduction

2.1. Observations with the Plateau de Bure interferometer

We have observed with the IRAM interferometer at Plateau de Bure (PdB, France) the emission of Frosty Leo in the rotational transitions ^{12}CO $J = 2-1$ at 1.3 mm (230.538 GHz) and ^{12}CO $J = 1-0$ at 2.6 mm (115.2712 GHz). This interferometer consisted of 5 antennas during these observations (February 2001) of 15 m in diameter with dual-band SIS heterodyne receivers (see `http://www.iram.fr`). Configurations 5C2 and 5D were used, with the projected baselines ranging from 15 m to 176 m. Due to the large extent of this source in the optical, up to ∼27″, we made a mosaic using observations with two different field centers; one at the center of the south optical lobe, at the offset position (2″, −5″) with respect to the initially assumed nebula center (coordinates J2000: $9^{\rm h}39^{\rm m}54\overset{\rm s}{.}00$, $+11°58'53\overset{''}{.}0$), and the other at the center of the north lobe, at the offset position (−2″, 5″). The observations were performed over a total period of five days. Different flux calibrators were observed the different days, like 3C 273, MWC 349 and CRL 618. We checked that the fluxes measured all days for all calibrators are consistent, within an uncertainty range of a 15% (25%) at 3 mm (1 mm). The calibration was performed in the standard way with the GILDAS software package. The sources 0851+202 and J 1018+055 were observed for the phase and amplitude calibration, and 0415+379 and 3C 273 for the passband calibration. We followed the standard reduction procedure for mosaics, including the correction for primary beam attenuation. The widths and position angles (PA) of the major axes of the CLEANed beams (at half-power level) are, respectively, $2\overset{''}{.}0 \times 1\overset{''}{.}7$ and 8° for the CO $J = 2-1$ maps, and $4\overset{''}{.}0 \times 3\overset{''}{.}0$ and 22° for the CO $J = 1-0$ maps. The conversion factors from flux units to main-beam brightness temperature ($T_{\rm mb}$) units are 6.7 K per Jy beam^{-1} and 7.6 K per Jy beam^{-1} at 1.3 mm and 2.6 mm, respectively. We have averaged the initial velocity channels, with velocity resolutions of 0.4 km s^{-1} and 0.8 km s^{-1} at 1.3 mm and 2.6 mm, respectively, to get a final velocity resolution of 3.25 km s^{-1} for both lines. The final maps of CO $J = 2-1$ and $J = 1-0$ are shown in contours in Figs. 2 and 3, respectively. We have superimposed these contours on the optical image obtained with the HST by Sahai et al. (2000), in order to identify the optical counterparts of the molecular components detected in our maps.

We have estimated the possible flux lost in these interferometric observations by comparing the total flux detected with the spectra obtained at the nebula center using the 30 m IRAM radiotelescope at Pico de Veleta (PdV; see Bujarrabal et al. 2001). We checked, using raw single-dish mapping, that these PdV profiles contain all the nebular CO emission. We have integrated the PdB intensity detected in each channel, which we have expressed in units of $T_{\rm mb}$ for PdV using the appropriate conversion factor. In Fig. 5 (see the electronic version) we show the profiles obtained from the PdB interferometer in comparison with those of PdV. The profiles are found to be very similar for all the velocity channels, for both transitions, except for a few minor differences. For CO $J = 1-0$, there is an intensity difference of ∼20% between the PdV and PdB profiles. This is probably due to the fact that the flux calibration is slightly inconsistent in both observations, since the PdB profile is the most intense and the intensity difference is constant for all velocities, except for a few channels at about 35 km s^{-1}. In these channels, the PdV profile shows a negative contribution, which is not detected in the

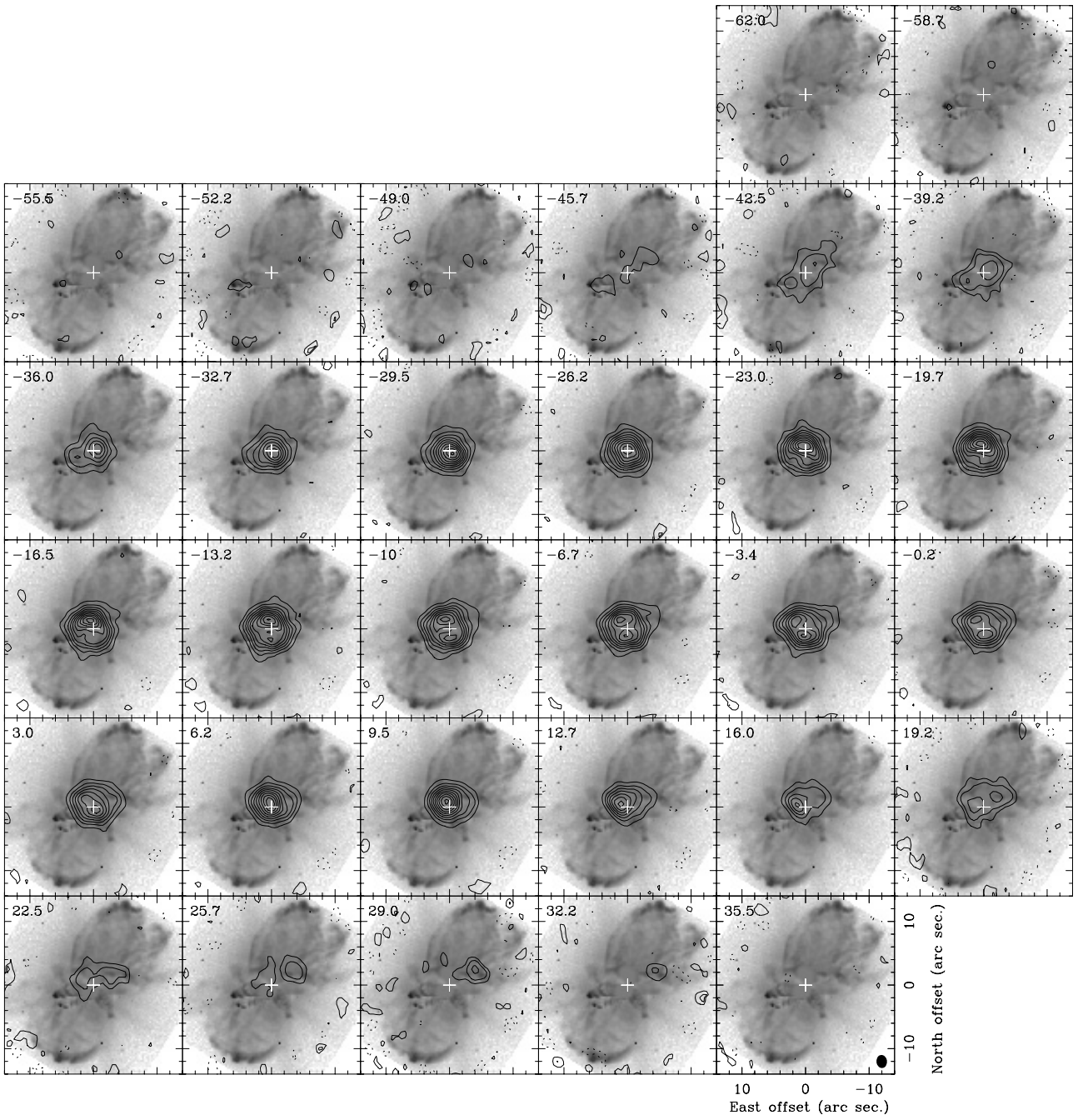

Fig. 2. In contours, we show PdB maps of ^{12}CO $J = 2-1$ emission from Frosty Leo (J2000 central coordinates: $9^{h}39^{m}53^{s}.99$, $+11°58'52''.8$), for the LSR velocities indicated in the left-upper corner of each box. The contours are superimposed on the optical image of the nebula. We deduce a systemic velocity of ~ -10 km s^{-1}. For the channels with velocities between -37 and 17 km s^{-1}, the first contour and the level step, in main-beam temperature units, are 0.54 K (80 mJy/beam). For the rest of channels the first contour is 0.27 K (40 mJy/beam), the second 0.54 K (80 mJy/beam), and from then the level step is 0.54 K. A negative level, equivalent to the first positive one, is shown in dashed contours. The CLEANed beam (at half-power level) is drawn in the right-bottom corner of the last panel.

interferometric observations, and which could result from a poor baseline subtraction in the PdV profile.

No continuum emission has been detected at the CO $J = 1-0$ or the CO $J = 2-1$ maps above a noise (1 rms) level of 0.6 and 1 mJy beam^{-1}, respectively. These limits were obtained by averaging all the channels that did not present line emission, up to a total bandwidth of 510 and 440 MHz at 3 and 1 mm respectively.

2.2. Observations with the OVRO Interferometer

We have also obtained high-angular resolution maps of ^{12}CO $J = 1-0$ emission (at 115.27 GHz) in Frosty Leo, using the millimeter interferometer of the Owens Valley Radio Observatory (OVRO), which consists of six 10.4 m-diameter antennas. Observations were performed in February and March 2001 in three different runs, using all the six antennas arranged in three different configurations, low (L),

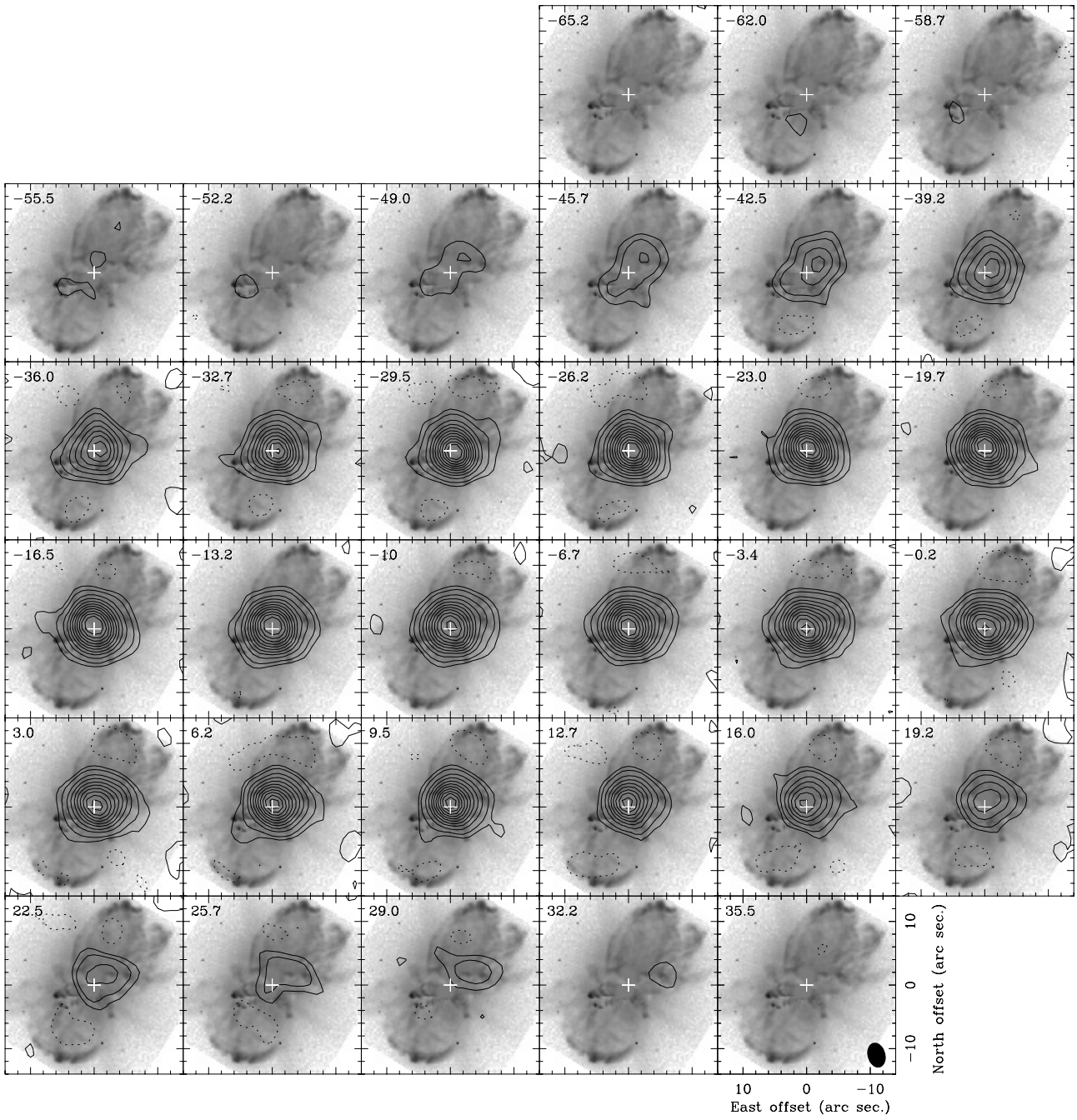

Fig. 3. In contours, we show PdB maps of ^{12}CO $J = 1-0$ emission from Frosty Leo, for the LSR velocities indicated in the left-upper corners. These contours are superimposed on the optical image of the nebula. The first level, in main-beam temperature units, is 0.23 K (30 mJy/beam) and the second 0.46 K. Thereafter the level step is 0.46 K (60 mJy/beam). A negative level is shown at −0.23 K with dashed contours. The CLEANed beam (at half-power level) is drawn in the right-bottom corner of the last panel.

equatorial (E), and high (H). Two additional H half-tracks were obtained in December 2002. The projected baselines between antennas ranged between 14 m and 241 m. We used the 3 mm SiS receiver operated in double side band mode. The calibration of the data was performed using the MMA software package[1]. Data were gain-calibrated using the quasars J 0851+202 and J 0854+201. The quasars 3C 273 and 3C 84 were used as passband calibrators and also as primary flux calibrators. Reconstruction of the maps from the visibilities was done using the Multichannel Image Reconstruction, Image Analysis and Display (MIRIAD) software. We Fourier transformed the measured visibilities with robust weighting (which is an optimized compromise between natural and uniform weighting) and forcing the channel spacing in our OVRO CO $J = 1-0$ data cube to be equal to that in our PdB maps. After that, data were cleaned and maps restored. The CLEANed beam for CO $J = 1-0$ have a width (at half-power level) of $2\farcs70 \times 1\farcs85$ and is oriented at PA $= -89.7°$. The conversion factor from Jy beam^{-1} to

[1] MMA is written and maintained by the Caltech's Millimeter Interferometry Group.

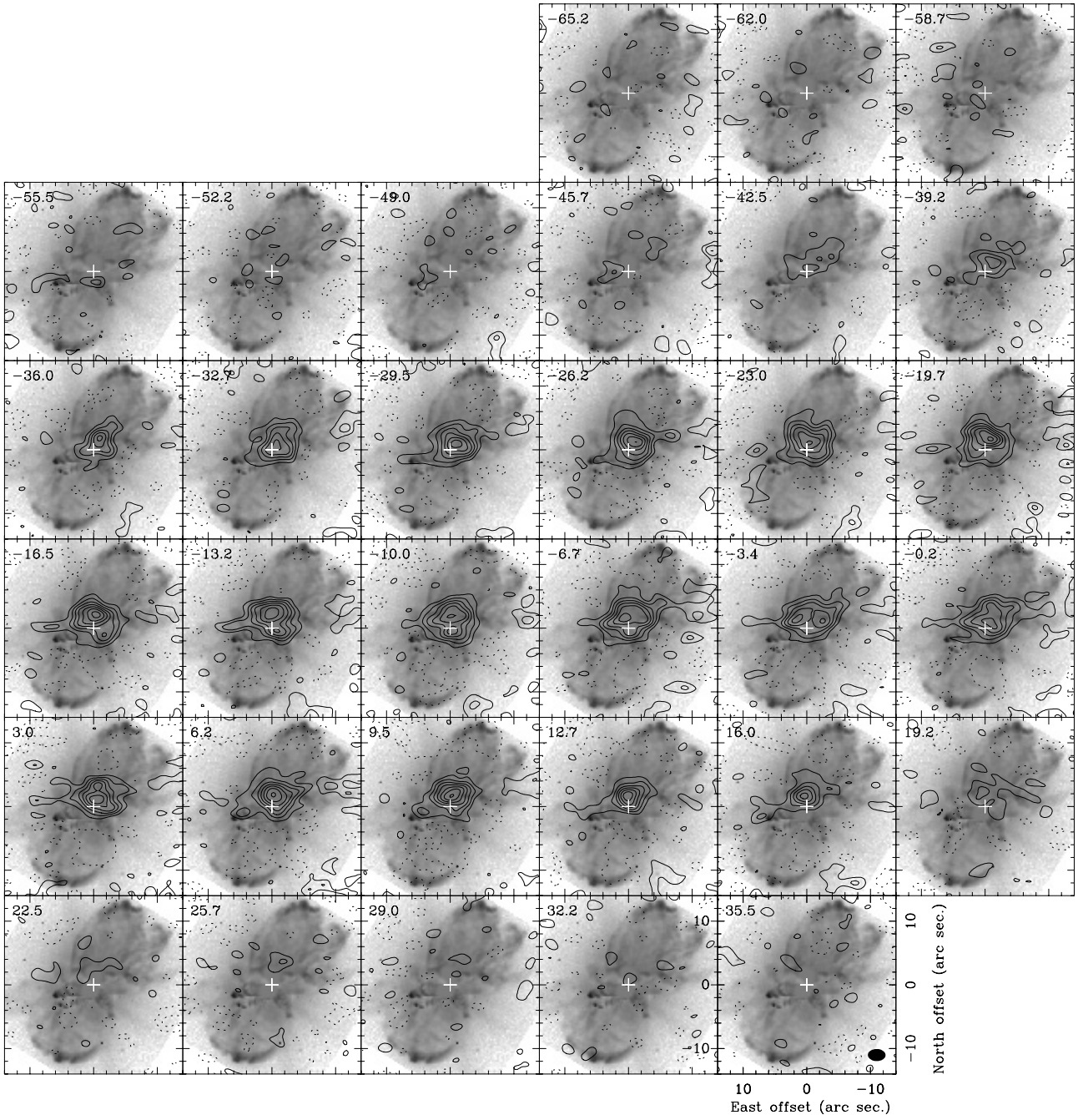

Fig. 4. In contours, we show OVRO maps of ^{12}CO $J = 1-0$ emission from Frosty Leo (same central coordinates as for PdB maps), for the LSR velocities indicated in the left-upper corners. Those contours are superimposed on the optical image of the nebula. The first level and the level step, in main-beam temperature units, are 1.05 K (60 mJy/beam). A negative level is shown at −1.05 K with dashed contours. The CLEANed beam (at half-power level) is drawn in the right-bottom corner of the last panel.

temperature units is 18.5 K per Jy beam^{-1}. The final maps are shown in contours in Fig. 4, superimposed on the optical image by Sahai et al. (2000).

By comparison with the CO $J = 1-0$ PdV data, as it is described in Sect. 2.1 (see Fig. 5 in the electronic version), we find that there are no significant flux losses in the OVRO data from the extended nebular components. Note, however, that some weak compact features are lost within the limited dynamical range (as seen by comparison with Figs. 2 and 3, and in Fig. 5).

3. Analysis of the CO maps

3.1. ^{12}CO $J = 2-1$

The CO $J = 2-1$ maps have a spatial resolution of $2\farcs0 \times 1\farcs7$, and a sensitivity limited by a maximum dynamical range of 9−10 (measured in the panels with brightest structures). The molecular envelope of Frosty Leo is very compact, with most of the emitting gas lying within a region of size ∼6″, in contrast to the much larger extent of the optical nebula, ∼27″.

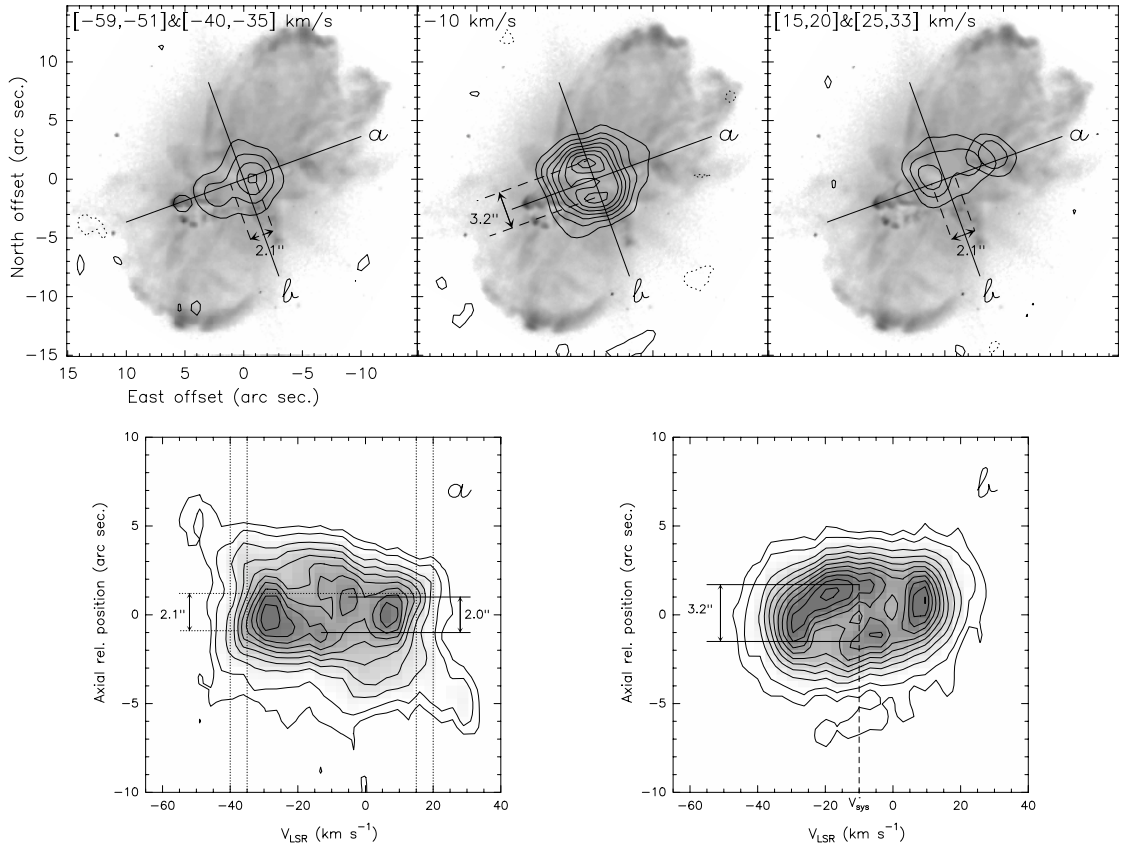

Fig. 6. *Upper* plots present in contours the average of the intensity detected for CO $J = 2-1$ from Frosty Leo, for the velocity ranges shown in the left-upper corner, over the optical image obtained by the HST. Velocity ranges has been chosen to best identify the ring (central nebular emission) and the jet features (elongated along the symmetry axis) in the complex nebula maps. In the left and right plots, the compact clumps at the extreme of the jets correspond to the ranges of highest expansion velocity. The central plot coincides with that shown in Fig. 2 corresponding to the systemic velocity. *Below*, for the same transition, the position-velocity diagrams of the emission detected along axes *a* and *b* are shown. Contours indicate the same level steps as shown in Fig. 2.

(PdV data confirm that the molecular distribution is very compact; see Sect. 2.1.) The systemic velocity of the nebula is ~ -10 km s^{-1} (LSR). We deduce the presence of a central ring or disk, with a symmetry axis at a PA in the sky plane of $\sim 110^{o}$, from the relative minimum observed along this axis at the central channels, between -13 and -3 km s^{-1}. CO emission from this central ring is detected in the channels with velocities between ~ -40 and 22 km s^{-1}. In the channels corresponding to the highest expansion velocities, in particular those within the velocity ranges [−59, −35] and [+15, +33] km s^{-1}, apparently the CO emission is distributed along the symmetry axis of the central ring (see upper plots in Fig. 6). This symmetry axis seems to coincide with the direction of the jets J1 and J1′ identified in the optical image (see Fig. 1 in the electronic version and Sahai et al. 2000), and is therefore very different from the main symmetry axis of the optical nebula. Note that, approximately at the offset positions ($-1\farcs0$, $+0\farcs4$) and ($+1\farcs0$, $-0\farcs4$) of the channels at ~ -39 km s^{-1} and at ~ 19 km s^{-1}, respectively, ring emission is detected at the highest velocity (with respect to the systemic one) on the opposite side of the jet contribution; this is characteristic of a gas distribution composed of a ring and two jets distributed along the ring symmetry axis (see e.g. Castro-Carrizo et al. 2002). However, in the channels with velocities between -13 and -23 km s^{-1} there is an intense maximum, located at the position (0″, 1″), which is not expected from an expanding homogeneous ring. A less-intense counterpart to this maximum (in the velocity domain, with respect to the systemic velocity) is found close to the nebula center, in the range between 3 and 10 km s^{-1}. Both maxima seem to come from compact structures, placed apparently along the (main) symmetry axis of the optical nebula, close to the central star; the one at the north seems to coincide with the component B_N identified in the visible (see Fig. 1 in the electronic version), although note that no molecular emission has been detected where B_S is detected in the optical.

In Fig. 6 we show in contours the CO $J = 2-1$ emission averaged over different velocity ranges, and superimposed on the optical image of the nebula. Position-velocity diagrams along the axes *a* and *b* are shown just below in Fig. 6, with axis *a* being the symmetry axis of the central ring projected on the sky plane, and axis *b* that perpendicular to *a*. Note that apparently axis *a* traces the direction followed by jets J1 and J1′ (see Fig. 1).

In order to estimate the inclination (i) of the symmetry axis of the molecular nebula with respect to the sky plane, we compare the true diameter of a "typical" ring in the central ring-like distribution, measured along axis *b* at the systemic velocity, with its projection on the plane of the sky, measured along

axis a. These lengths are related by the sine of i, assuming that the ring gas distribution is perfectly axially symmetric. A "typical" ring could be defined by intensity peaks in both position-velocity diagrams (e.g. Castro-Carrizo et al. 2002). In diagram b (right-bottom plot of Fig. 6) we estimate a diameter for the "typical" ring of $\sim 3\farcs2$, which is the angular distance between the maxima at the systemic velocity (upper-central plot of Fig. 6). Along axis a, however, the determination of the projection of the "typical" ring is more difficult, due to the contribution of several intense components (apparently close to the nebula center, as mentioned before). Let us constrain its value: In diagram a (bottom-left plot of Fig. 6) the distance between the marked relative maxima, $\sim 2\farcs0$, seems to be a lower limit, since their expansion velocity (~ 5 km s^{-1}) is very small in comparison with the maximum of ~ 30 km s^{-1}. On the other hand, the outermost emission from the ring is detected along axis a in the channels at $[-40, -35]$ km s^{-1} and $[+15, +20]$ km s^{-1} (Fig. 2), the angular distance on axis a between their maxima being $\sim 2\farcs1$ (marked in the right-upper and left-upper plots of Fig. 6, and in diagram a). The projection of the "typical" ring diameter on axis a seems therefore well constrained between $2\farcs0$ and $2\farcs1$. So, from the ratio between the measured ring diameter (on axis b, $\sim 3\farcs2$) and its projection on the plane of the sky (on axis a, $\sim 2\farcs0$), we deduce that $|i| \sim 40° \pm 5°$. At a PA of 110°, the symmetry axis of the molecular ring-like structure is inclined therefore $i \sim -40°$ with respect to the sky plane, i.e. the easternmost jet is the closest to us.

Ring emission has been detected in the channels with velocities between -40 km s^{-1} and 20 km s^{-1}, implying that gas in the ring is expanding at projected velocities $\lesssim 30$ km s^{-1}. On the other hand, the molecular emission detected along the symmetry axis expands at projected velocities between ~ 25 and 45 km s^{-1}. So, the maximum expansion velocity detected in CO for these outflows is ~ 70 km s^{-1}, if we assume that $i = -40°$.

As mentioned before, in Fig. 2, we find an absolute intensity maximum in a compact region located in the north lobe, with expansion velocities (projected in the line of sight) between -23 and -13 km s^{-1}. This brightest molecular feature apparently is within the region B_N of the optical nebula (Fig. 1 in the electronic version). However, if we assume that B_N is placed along the main axis of the optical nebula, it is expected its expansion velocity to be redshifted, which contrasts with the blueshifted velocities of the molecular component. Note that an inclination for the (main) symmetry axis of the optical nebula of 16° with respect to the sky plane is adopted (Lopez et al. 2001), the south lobe being the closest to us. In addition, since our assumption that B_N is located along the main axis could be wrong, we cannot definitely rule out that it is the optical counterpart of the brightest molecular feature. In Sect. 5 we analyze the possible origin of these intense CO components.

3.2. ^{12}CO $J = 1-0$

We have obtained data of the ^{12}CO $J = 1-0$ transition with the PdB and OVRO interferometers; see Figs. 3 and 4, respectively. The OVRO maps have higher spatial resolution (of $2\farcs7 \times 1\farcs9$) than the PdB ones, but the PdB data have higher dynamical range (20 in the channels with the brightest features). In comparison with the ^{12}CO $J = 2-1$ maps, the higher sensitivity of the PdB CO $J = 1-0$ data allows us to detect emission from faster (weaker) components. In particular, the highest expansion velocity detected for the jets is ~ 75 km s^{-1}, for $i = -40°$, which is higher than that detected in CO $J = 2-1$, ~ 70 km s^{-1}. In general, the PdB CO $J = 1-0$ maps allow us to confirm the structure inferred from the CO $J = 2-1$ data.

From the OVRO data, we can analyze the structure of the nebula in more detail. In particular, these observations allow us to confirm the ring-like central structure in the low-velocity panels, and the gas distribution along the optical jets in the channels corresponding to high expansion velocities. The intense components observed in the CO $J = 2-1$ maps, in the velocity ranges $[-13, -23]$ km s^{-1} and $[+3, +10]$ km s^{-1}, are also detected. However, due to sensitivity limitations, we must be cautious in our analysis of new features not seen in the CO $J = 2-1$ maps. Note, for example, the features found in the velocity ranges $[-30, -23]$ km s^{-1}, $[-17, -13]$ km s^{-1} and $[+9, +16]$ km s^{-1}; they could come from additional jets, maybe on the opposite side of the nebula. Moreover, these elongations at about -30 and 7 km s^{-1} are also tentatively detected in the PdB CO $J = 1-0$ maps, their weakness in the PdB maps might be due to a dilution effect by the larger beam.

3.3. Modeling; estimate of the physical parameters

We have developed a numerical code similar to that described in Bujarrabal et al. (1997, 1998) in order to model the spatio-kinematical distribution of the molecular component of Frosty Leo (see Sect. 3.1). The model predictions for both transitions, ^{12}CO $J = 2-1$ and 1–0, are compared with the observations, which allows us to estimate the excitation conditions (density, temperature) of the emitting gas. Note that we have adopted a simplified description of the CO excitation by assuming a single rotational temperature, which varies within the nebula. The code takes into account the opacity effects and the radiative interaction. The predicted emission is convolved with the CLEANed beam of the observations. A CO abundance (with respect to H_2) of 2×10^{-4} and an inclination of the symmetry axis of the ring with respect to the sky plane of $-40°$ (estimated in Sect. 3.1) have been assumed. In this analysis $D = 3$ kpc is adopted. In Sect. 6 we study how a change in the assumed distance would influence our conclusions.

In order to satisfactorily fit the detected emission for both transitions, CO $J = 2-1$ and $J = 1-0$, we adopt a spatial distribution, shown in Fig. 7, composed of: 1) a central ring with a very dense inner region and a more tenuous outer distribution; 2) two cone-shaped jets, whose symmetry axes coincide with the symmetry axis of the central ring. An inner hole at the nebula center elongated along the symmetry axis is necessary to fit the inner CO emission structure in our maps. Cone-shaped jets fit the data slightly better than cylindrical jets.

In order to estimate the nebular density, we also take into account the molecular mass deduced from previous ^{13}CO $J = 1-0$ data, since this emission is optically thin.

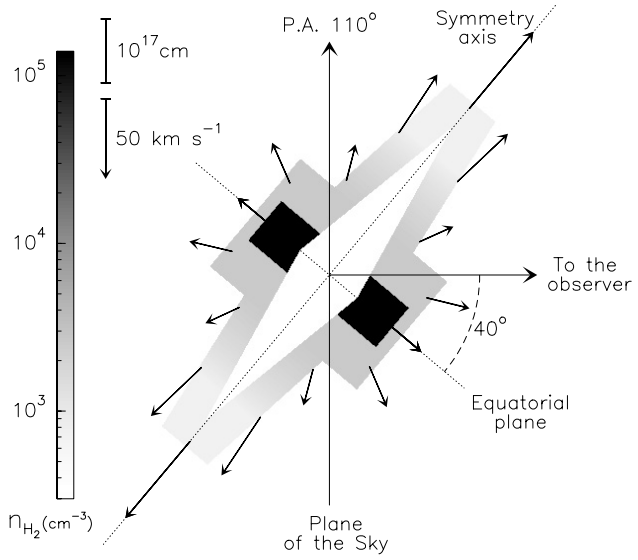

Fig. 7. Model of the molecular nebula whose emission fits our maps of ^{12}CO $J = 2-1$ and $J = 1-0$. The velocity field is presented by arrows. The spatial and density scales are also shown.

We find that the density of the central ring cannot be uniform. In particular, our best fit is obtained when the central ring is composed of a dense inner region, of density 1.4×10^5 cm^{-3}, and a much more tenuous outer region, of density 2.5×10^3 cm^{-3}. The density of the inner region (whose emission is very opaque) has been chosen such that the total molecular mass coincides with the value deduced from ^{13}CO $J = 1-0$; Bujarrabal et al. (2001) obtained 0.9 $M_\odot$ for $T_{\rm rot} = 15$ K, and following the same method we deduce 0.8 $M_\odot$ for an adopted $T_{\rm rot} = 10$ K. If we assume a density higher than 2.5×10^3 cm^{-3} in the outer region of the ring, this results in too sharp a boundary of the ring intensity distribution, which is not observed.

The fact that the opacity is very high at the nebula center is also supported by the different ratios of the ^{12}CO and ^{13}CO lines obtained for different velocity ranges (see Bujarrabal et al. 2001). Note that the profiles of both ^{12}CO lines are similar, but different to those of ^{13}CO. The unusually low ^{12}CO/^{13}CO line ratio could also result from the high opacity of the ^{12}CO emission in Frosty Leo. This high opacity makes it very difficult to estimate abundances from the observations, hence we have assumed a typical ^{12}CO abundance for PPNe.

Since the density of the outer tenuous region of the ring and of the jets is very low, between 2.5×10^3 and 0.7×10^3 cm^{-3}, the photodissociation caused by interstellar photons could have played an important role in these outer nebular regions (as, perhaps, in the lobes of the optical nebula, which are not detected in CO emission). From the calculations of van Dishoeck & Black (1988) we have estimated the CO lifetime expected in these regions, using the thicknesses and the densities deduced in the nebula. We have obtained a CO lifetime of ∼500 yr for the outer region of the ring and of ∼400 yr for the tips of the jets; both values are much smaller than the estimated kinematical lifetime of the jets (see Sect. 4.1), ∼1700 yr for a distance of 3 kpc. This confirms that CO photodissociation is significant in these tenuous regions. Therefore, the densities of these diffuse regions are probably strongly underestimated in our model. However, the effects of photodissociation are expected to be negligible in the inner dense region of the ring, for which the CO lifetime is $\sim 10^6$ yr.

We have supposed that the cone-shaped jets have inner empty cones as extensions of the central nebular hole. For a good fit these inner empty cones cannot be much larger than assumed. Note that the density of the jets would be (slightly) lower if no empty cone-shaped regions were assumed.

A constant rotational temperature of 10 K is adopted for the whole nebula, in order to reproduce the intensity ratio of both transitions. This low temperature (15 K is usually assumed for PPNe) is comparable to that deduced by Sahai et al. (2000) from ^{13}CO/^{12}CO line ratios, ∼11 K. Small changes (of just 2 K) are incompatible with the intensity ratio observed for both transitions. According to discussions by Bujarrabal et al. (1997), thermalization cannot be assumed in the least dense regions, that is, the jets and probably the outer part of the ring. In the densest regions, however, the kinetic temperature probably coincides with the rotational temperature.

For the assumed geometry, we obtain an expansion velocity for the jets that increases from 20 to 70 km s^{-1}, consisting of a radial component with a constant modulus of 20 km s^{-1}, and an axial component (along the symmetry axis of the molecular nebula), which increases linearly from 0 to 50 km s^{-1} from the inner to the outer part of the jets. In the ring, the expansion velocity has a radial component increasing (with radius) from 15 to 22 km s^{-1}, and a minor axial one increasing from 0 to 6 km s^{-1} from the nebula center. Note that this expansion velocity for material in the central ring (ranging from 15 to 27 km s^{-1}) is high in comparison with the values typical of most AGB envelopes ($\lesssim$15 km s^{-1}). (A local velocity dispersion of 4 km s^{-1} is assumed, since this value produces the best fit to the data.)

In Fig. 8 the predictions for the CO $J = 2-1$ emission from this model are shown. In Fig. 9, in the electronic version, plots predicted by modeling equivalent to those of Fig. 6 are shown. We conclude that this gas distribution, with a ring and two jets expanding from it along its symmetry axis, satisfactorily reproduces the main features of the detected emission, except for the compact and very intense components detected between ∼3 and 10 km s^{-1}, and between ∼−13 and −23 km s^{-1}. It is likely therefore that the density distribution of the ring is in reality more complex than that assumed in the model.

4. Kinematical post-AGB lifetimes and dynamical parameters

4.1. Kinematical post-AGB lifetimes

Two kinematical post-AGB lifetimes in principle can be estimated from high-resolution mapping: 1) the time elapsed since the copious mass loss that is characteristic of the late AGB phase ceased, and 2) the time since the wind interaction, characteristic of the PPNe, took place. In order to estimate 1), one can use the emission coming from the central ring, since in most PPNe it has not been altered by the post-AGB ejections. However, it seems (see Sects. 4.2 and 5) that in Frosty Leo

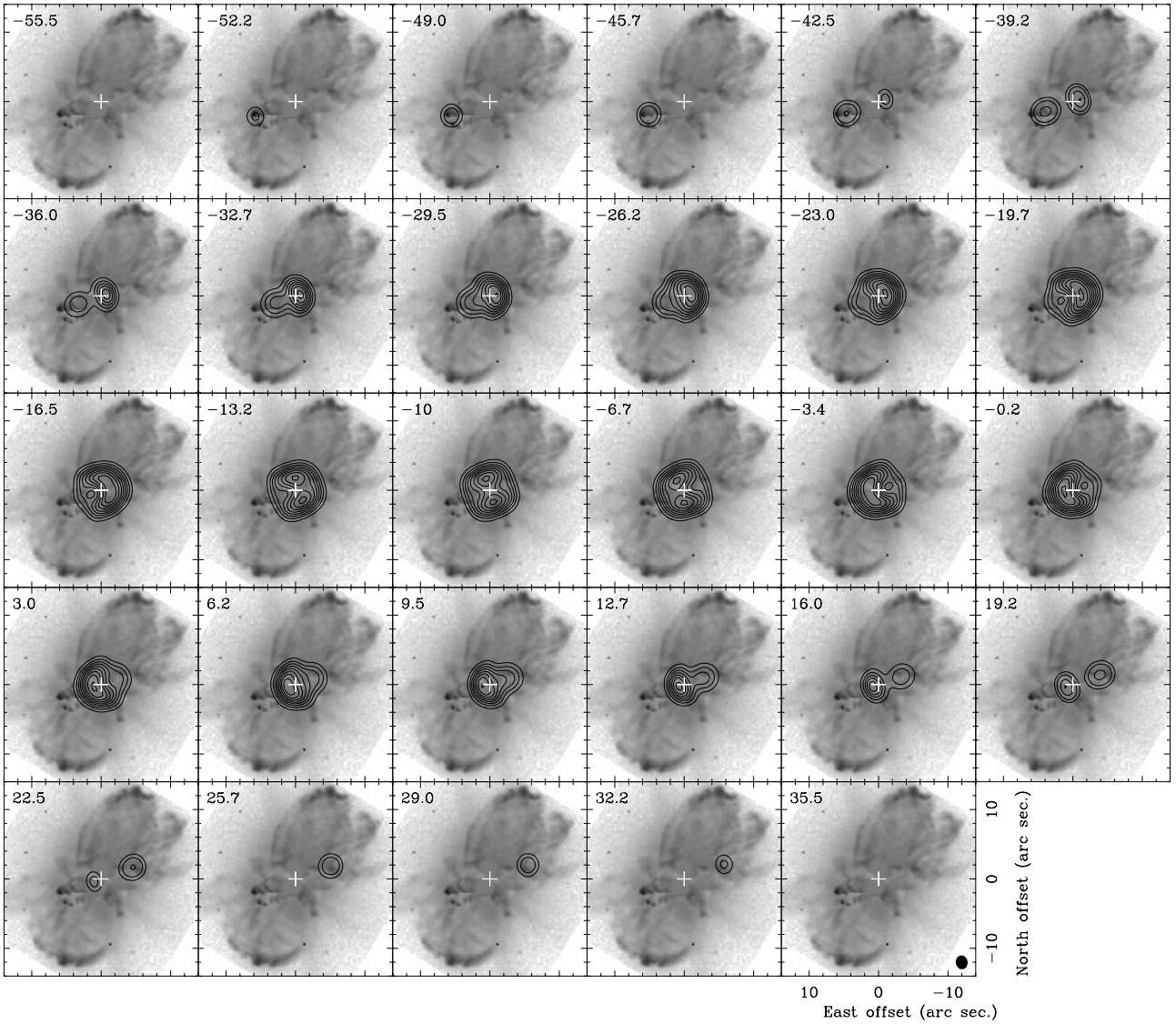

Fig. 8. Predictions for the ^{12}CO $J = 2{-}1$ emission coming from a spatio-kinematical nebular model, composed of a ring and two jets ejected along the symmetry axis of the ring, which is inclined $-40°$ with respect to the sky plane, at a PA of 110°. Note that this symmetry axis does not fit with the symmetry axis of the optical nebula. The same velocity channels and contours as those in Fig. 2 are shown. The brightness temperature obtained by the model has been convolved with the CLEANed beam obtained in the analysis of the data.

(at least) part of this central ring could have been accelerated by post-AGB outflows. In this case, the time elapsed since the AGB mass loss ceased cannot be easily determined. We have therefore not used this inner central emission to estimate kinematical post-AGB times.

We can estimate, however, the lifetime of the detected fast axial outflow. For the measured inclination (in Sect. 3.1), the tips of the jets are at a radial distance of $\sim 3.8 \times 10^{17}$ cm from the nebula center, and they expand at ~ 70 km s^{-1}. We obtain therefore a kinematical lifetime for the jets of ∼1700 yr. This is a long time in comparison with those found for most post-AGB winds (often less than 1000 yr; Bujarrabal et al. 2001), but consistent with the absence of shocked gas emission lines in the optical and near infrared; see e.g. Morris & Reipurth (1990). Since a single interaction followed by free expansion is assumed, this post-AGB lifetime could be underestimated if some acceleration had occurred during the post-AGB phase, or overestimated if interaction with outer gas had taken place. Note, however, that an underestimate larger than a factor of two is not expected (which is obtained for a constant, still present acceleration), and that an important overestimate is not expected either, since a large dense halo has not been detected.

The relation between the evolution of the star and the onset of the fast post-AGB winds is not well understood. For example, in the case of AFGL 618, the central star is quite hot (spectral type B0), but the kinematical lifetime of the most recent high-velocity post-AGB winds is <100 yr (Sánchez Contreras et al. 2004). In contrast, although the central star of Frosty Leo is relatively cool (with an effective temperature of ∼3700 K), its post-AGB winds started a long time ago, at least 1700 yr ago (see Sect. 5.1), which is of the order of (or even larger than) the typical time required by a star to evolve from the AGB to the PN phase.

These kinematical lifetimes have been derived for D = 3 kpc. Given our uncertainty in determining the real distance (which has been constrained to lie between 1 and 4 kpc; Mauron et al. 1989), we can expect that kinematical times of the molecular components range between 600 yr and 2300 yr, for both these extreme cases, our main conclusions still remain valid; see Sect. 6.

4.2. The dynamics of the different nebular components

We have determined the "scalar momentum" (P) and the kinetic energy (E) of the different nebular components, from the spatio-kinematical model that best fits the data. These parameters are obtained by integrating $\rho \times v$ and $\rho \times v^2/2$, respectively, in each region of the nebula, where ρ is the denstity and v the velocity modulus at each point of the nebula. Note that we are calculating a "scalar" momentum, that is, the scalar sum of all the momentum moduli of each region. The mass of the jets and of the tenuous part of the ring have been derived from our model, whereas the mass of the thick central region within the ring has been deduced from analysis of ^{13}CO data, since the ^{12}CO emission is optically very thick (see Sect. 3.3). So, we obtain that M, P and E for the central ring are, respectively, 0.8 $M_\odot$, 4×10^{39} g cm s^{-1} and 4×10^{45} erg, and for the jets are 0.01 $M_\odot$, 6×10^{37} g cm s^{-1} and 10^{44} erg.

Note that although the model does not reproduce the exact location of the most intense components of the nebula, observed at ∼[+3, +10] km s^{-1} and ∼[−13, −23] km s^{-1}, it reproduces most of the intensity in those channels. So, even if the density distribution assumed in our model is relatively simple, it supplies satisfactory estimates of the dynamical parameters for the detected molecular nebula.

However, as we have mentioned in Sect. 3.3, photodissociation could have played an important role in the most tenuous regions of the nebula, i.e., the jets and the outermost regions of the ring. Therefore we probably underestimate the dynamical parameters of Frosty Leo. In order to evaluate the photodissociation effects, we take into account the decrease of the nebular density (as r^{-2}, r being the radius) during the expansion of the nebula. We find that photodissociation became significant in the diffuse regions in the last 600 yr. By comparison with the CO lifetimes estimated in Sect. 3.3 for these tenuous regions (which carry ∼6% of the total nebular mass) we conclude that we may underestimate the total mass of these tenuous regions by a factor 2–3. In this case, the total nebular mass would be underestimated by ∼11%, and the energy only by ∼12% (due to the low mass carried by the jets). For the optical lobes, where we do not detect any CO emission, we cannot quantitatively estimate the amount of mass which is unaccounted for. So, we are probably significantly underestimating the values of the dynamical parameters.

It is remarkable that the bulk of the gas accelerated in the post-AGB phase of Frosty Leo is placed in the central ring, which reaches expansion velocities of up to ∼30 km s^{-1}. The detected molecular jets represent, however, a very small portion of the whole nebula, even if we take into account the photodissociation effects discussed above. Therefore, the important momentum excess found for Frosty Leo ($\frac{P}{L/c} = 2 \times 10^5$ yr, independent of distance), when compared with the maximum linear momentum available from radiation-pressure (see Bujarrabal et al. 2001), is carried by the accelerated central ring, instead of the molecular jets (in contrast to other well-studied PPNe). The mechanism that accelerated the central molecular envelope of Frosty Leo was not just the radiation pressure, but likely mainly the interaction with post-AGB ejections.

5. Comparison between the molecular maps and optical imaging

5.1. Interpretation of the shape and the shaping of Frosty Leo

We first analyze the reason why the symmetry axis of the molecular ring (with $i \sim -40°$ and PA ∼ 110°) is significantly inclined with respect to the (main) symmetry axis of the optical nebula (with $i \sim -16°$ and PA ∼ 150°, Lopez et al. 2001); the angle between both axes is ∼42°. Note that, to date, the low-velocity CO emission in most of the well-studied PPNe (see, for example, M 2−56 or M 1−92; Castro-Carrizo et al. 2002 and Bujarrabal et al. 1998, respectively) mainly comes from a central disk or torus, perpendicular to the symmetry axis of the optical nebulae. This massive component is interpreted as the remnant of the AGB envelope that has not been accelerated by the post-AGB ejections, which took place along the symmetry axis. In principle, the molecular component of Frosty Leo shows a similar structure: a ring-like structure perpencular to two fast jets. However, in this case neither the jets nor the ring seem to be related to the main symmetry axis of the optical bipolar nebula. Moreover, no emission is detected from the large lobes of the optical nebula. We interpret this absence of molecular emission in the optical lobes as a result of CO photodissociation caused by interstellar photons, which seems to be significant in the less-dense regions of the molecular nebula (see Sect. 3.3). Note that the density of the (likely dissociated) gas in the optical lobes is probably lower than that in the molecular lobes, since higher dispersion is expected farther from the central star.

Since the molecular distribution is much smaller than the optical nebula and does not seem to be significantly affected by the ejection that resulted in the main optical lobes (see also Sect. 5.2), we suggest that the molecule-rich jets J1 and J1′ were ejected later than the ejection responsible for the main bubble-like lobes, seen in the optical. Note, moreover, that from the velocities given by Phillips & Cuesta (1997) and Dougados et al. (1992), we can crudely derive kinematical lifetimes for the main optical lobes between 2500 and 3500 yr. (In particular, the lifetime of 3500 yr has been derived at 4–5″ from the star; moreover the data indicate an increase of the expansion velocity with the distance to the center, as happens in many other PPNe, in which the lifetime estimates do not almost depend on the point at which the velocity is measured.) Frosty Leo would be therefore the result of multiple post-AGB ejections: 1) A first ejection took place yielding the primary bipolar structure seen in the optical. 2) Later, multiple ejections detected in the visible (J1, J2, J3, J1′ and J2′; see Fig. 1) bored holes in the

previous matter distribution and, in general, significantly modified the geometry of the inner nebular regions, which became more complex. The result of events (1) and (2) above would be a ring-like structure perpendicular to the most recent ejections, with a complex density law resulting from multiple (possibly non-simultaneous) shock interaction episodes. This could explain why we find massive clumps which do not appear to be directly related to the ring or the jets. In addition, note that the expansion velocity measured in the ring is unexpectedly high. (Observations of most PPNe show that the ring perpendicular to the post-AGB ejections mainly keeps the kinematics of the previous AGB phase, with expansion velocities of $\sim$10 km s^{-1}. The maximum expansion velocity measured within the central molecular ring of Frosty Leo is however $\sim$30 km s^{-1}.) It seems therefore that the material which now resides in the molecular ring-like structure was also accelerated during the post-AGB phase.

Finally, we note that Frosty Leo shows some properties in common with CRL 2688, and which so far have not been found in other PPNe and PNe. CO maps of CRL 2688 (see Cox et al. 2000) show the contribution of multiple high-velocity outflows along very different directions; a main outflow is expanding along the (main) symmetry axis of the nebula, and low-mass jets are flowing at high velocity approximately in the equatorial plane. In addition, Cox et al. find a central "shell-like" structure not aligned with any of the outflow axes, and which could be tracing the most recent episode of mass-loss in this object.

5.2. Differences between the structures deduced from the molecular maps and from optical imaging

We have found no clear signatures of the first ejection (along the main symmetry axis of the optical nebula) in our CO maps, therefore at the spatial scale at which CO is detected. We have checked that introducing an empty region in our model along the main symmetry axis of the optical nebula (assuming PA = 150° and $i = -16°$; Lopez et al. 2001) neither improves our fit to the data nor sheds light on the origin of the compact intense clumps. This empty axial structure would result in an inclination of the symmetry axis of the central ring towards the main symmetry axis of the optical nebula, with respect to the jet axis, which is not observed. Moreover, it would result in moving the model intensity peaks in the channels at [−26, −13] km s^{-1} and [−7, +3] km s^{-1} further to the south-west and to the north-east, respectively, from their current location in our best-fit model, which is opposite to what is needed in order to fit the compact intense clumps detected in our maps. This last fact suggests that there might be an empty region along another axis, different to that traced by J1 and J1′, which could be responsible for the clumpy structure observed in the ring.

In particular, we have not found any signature of the flattened disk close to the star and perpendicular to the main optical lobes of the nebula, which is inferred from the optical and IR images. This could be due to the fact that the emission from such a very thin disk is diluted within our relatively wide telescope beam and/or that this emission is confused in our maps by the presence of other central bright components. As we have mentioned in the previous subsection, it is also possible that the very inner regions of such a disk have been affected by recent ejections of stellar material, particularly by those responsible for jets J1 and J1′, in such a way that it cannot be easily recognized in the present density distribution of the inner nebula.

We hope that future CO data with much higher resolution will make possible a more accurate determination of the actual molecular distribution, in order to compare it with images of dust scattered light, and so to properly analyze the history of the mass loss process in Frosty Leo.

6. Dependence on the distance and possible scenarios to explain Frosty Leo peculiarities

We now discuss how our main conclusions are affected by the relatively large uncertainty in the distance to Frosty Leo, which is believed to lie between 1 and 4 kpc (Mauron et al. 1989; see Sect. 1). If for this high-latitude source we can assume that the Galatic rotation model is valid, we derive a kinematical distance of 1.2 kpc using the rotation law of Goodrich (1991). However, given the probably limited validity of this model for high latitude sources, this estimate may not be very reliable. In Table 1 we present values of all distance-dependent paramenters derived in this work for 1, 3 and 4 kpc. Comparing these values, we note that:

1) The value of the luminosity obtained for 1 kpc, and even that for 3 kpc, is very low in comparison with what is observed in most post-AGB stars. It has been argued in different papers (see Sect. 1) that the luminosity of a post-AGB star should be >1500 $L_{\odot}$, or even >3000 $L_{\odot}$, while the most usual values are $\sim 6 \times 10^3$–10^4 $L_{\odot}$.

2) The ratio $\frac{P}{L/c}$ does not depend on the distance, so our conclusions regarding the momentum excess in Frosty Leo remain valid (Sect. 4.2).

3) The CO lifetimes derived from the calculations by van Dishoeck & Black (1988) do not depend on the distance, since such lifetimes are derived from observable column densities. However, our discussion of photodissociation effects does depend on D. For D = 1 kpc, the kinematical lifetime deduced for the jets is $\sim$600 yr, so comparable to the CO lifetime; it is not expected therefore that photodissociation (in the whole detected nebula) becomes important. In the other extreme, for D = 4 kpc, we would expect that photodissociation becomes slightly larger than for 3 kpc in the jets and the tenuous part of the ring, which, in any case, would only represent $\sim$10–20% of the total mass in the detected molecular component.

4) Note that even a kinematical lifetime of 600 yr (the minimum value deduced, from only the molecular component and for a distance of 1 kpc) seems too long a post-AGB lifetime if we take into account the relatively low temperature (3700 K) of the central star of Frosty Leo, only modestly higher than that of an AGB star. Considerably higher lifetimes are moreover obtained when considering the lifetimes derived from optical data (see Sect. 5.1) or by assuming larger distances (see Table 1). We can think of two possible scenarios to explain such a peculiarity: (A) The central star is of sufficiently low mass, so that its temperature increases only modestly during the long

Table 1. Parameters derived in this work for an assumed distance of 3 kpc in comparison with their values for 1 and 4 kpc. Discussion is presented in Sect. 6.

Distances (kpc)	1	3	4
Maximum (axial) extent (cm)	9×10^{16}	3×10^{17}	4×10^{17}
Particle density (cm^{-3})	4.2×10^5–2.1×10^3	1.4×10^5–0.7×10^3	1.1×10^5–0.5×10^3
Luminosity ($L_\odot$)	250	2250	4000
M ($M_\odot$)	0.09	0.8	1.4
P (gr cm s^{-1})	0.5×10^{39}	4.1×10^{39}	7.2×10^{39}
E (erg)	0.5×10^{44}	4.1×10^{45}	7.3×10^{45}
Kinematical post-AGB lifetime (yr)	570	1700	2300
Galactic altitude (pc)	373	1120	1490

post-AGB lifetime of Frosty Leo. Schönberner (1983), for instance, predicts that a star of initial mass 1 $M_\odot$ would increase its temperature 800 K in 100 yr, while the same increase would take 1000 yr for a star of initially 0.8 $M_\odot$. (B) The central star has resulted from a (kind of) "born-again" process (e.g. Blöcker & Schönberner 1997) that could account for a lower effective temperature, the long lifetimes obtained for its envelope, as well as a luminosity somewhat lower than for standard models.

5) The galactic altitude of Frosty Leo is extraordinarily high, and much higher when larger distances are assumed. Given the usual galactic altitudes of PNe and PPNe (according to Pottash 1984, ∼66% of AGB stars and PNe are below 250 pc), it would be reasonable to support the option of the lowest distance in our range, ∼1 kpc. Note that the high galactic altitude of Frosty Leo might be related to the low initial mass of its central star.

7. Conclusions

We have observed with the PdB interferometer the emission coming from Frosty Leo of the rotational transitions ^{12}CO $J = 2$–1 and 1–0, and with the OVRO array that of the ^{12}CO $J = 1$–0 transition. No significant flux loss has been found.

Our maps show that the molecular envelope of Frosty Leo is very compact (the bulk of which has a size of ∼6″, whereas the optical nebula has a size of ∼27″). We find that the emission comes mainly from a central ring-like structure with a symmetry axis inclined ∼−40° with respect to the plane of the sky, at a PA of ∼110°. High-velocity jets have been detected along the symmetry axis of this molecular ring, with velocities as high as ∼75 km s^{-1}. We find that the projection (on the sky plane) of the symmetry axis of the molecular distribution is oriented at about 40° from the (main) symmetry axis of the extended bipolar optical nebula. The molecular jets seem however to coincide with some jet-like features identified in the optical image.

We have developed a numerical code to model the spatio-kinematical distribution and the excitation conditions of the molecular envelope. We have found that the central ring is composed of a very dense inner component and a tenuous outer distribution, and that the jets are the most diffuse features. We have deduced a rotational temperature of 10 K. The gas of the central ring expands mainly radially with velocities from 15 to 27 km s^{-1}, and the jets expand mainly axially with velocities from 20 to 70 km s^{-1}. The model satisfactorily reproduces most of the detected emission, except for some compact protuberances detected within the central ring.

The high velocity of the central ring of Frosty Leo indicates that it is not the undisrupted remnant of the previous AGB envelope, but has been shocked by post-AGB ejections. At least two ejections have been identified in the nebula: a first one that could have shaped the optical main bipolar distribution and probably accelerated part of the molecular ring, and (at least) a later ejection (also seen in the visible, as secondary jet-like features), which would be mainly responsible for the current shape of the molecular nebula.

The kinematical lifetime of the molecular jets is ∼1700 yr (for an assumed D of 3 kpc), which is surprisingly long in comparison with the lifetimes obtained for the post-AGB winds of most PPNe, and even more so if we take into account the low effective temperature estimated for its central star (∼3700 K). In Sect. 6, different scenarios are proposed: either the central star is of relatively low mass or it is a "born-again" object.

We have estimated the mass, the "scalar momentum" and the kinetic energy of different nebular components from the model that best fits the data. For the central ring-like structure $M = 0.8\ M_\odot$, $P = 4 \times 10^{39}$ g cm s^{-1} and $E = 4 \times 10^{45}$ erg. For the jets $M = 0.01\ M_\odot$, $P = 6 \times 10^{37}$ g cm s^{-1} and $E = 1 \times 10^{44}$ erg. Photodissociation of CO may lead to underestimates of the total mass, momentum and energy in the detected molecular nebula, but by no more than 10–15%, although its effects are probably important for the jets as well as in the part of the nebula detected in the optical but not in mm-waveleghts. It is very remarkable that the bulk of the gas accelerated in the post-AGB phase of Frosty Leo is located within the central ring. The important momentum excess found in Frosty Leo, in comparison with the maximum available by the radiation-pressure mechanism, resides therefore in the central ring instead of the molecular jets (contrary to what is found in most PPNe). Several post-AGB shock interaction processes seem necessary to explain the complex structure of this nebula, and, in particular, the high amount of gas that is expanding at high velocity.

Acknowledgements. A.C.-C. was supported during the development of this work initially by the Spanish SEEU and the European Social Fund, and later by a Marie-Curie Intra-European Fellowship within the 6th European Community Framework Programme. CSC was supported by the American National Science Foundation

Grant No. 9981546 to OVRO. The contribution by VB and JA was funded during this work by the Spanish DGES, under project PB96−0104. RS acknowledges financial support from NASA through Long Term Space Astrophysics grant (No. 399-20-61-00-00) and HST/GO grant (No. GO-06816.01-95A) from the Space Telescope Science Institute. We thank Michael Bremer for his help in the preparation of Fig. 7. We acknowledge the IRAM staff (both at Plateau de Bure and Grenoble) and the OVRO staff for carrying out the observations and the help they provided during the data reduction.

References

Alcolea, J., Bujarrabal, V., Sánchez Contreras, C., Neri, R., & Zweigle, J. 2001, A&A, 373, 932
Blöcker, T., & Schönberner, D. 1997, A&A, 324, 991
Bujarrabal, V., Alcolea, J., Neri, R., & Grewing, M. 1997, A&A, 320, 540
Bujarrabal, V., Alcolea, J., & Neri, R. 1998, ApJ, 504, 915
Bujarrabal, V., Castro-Carrizo, A., Alcolea, J., & Sánchez Contreras, C. 2001, A&A, 377, 868
Castro-Carrizo, A., Bujarrabal, V., Sánchez Contreras, C., Alcolea, J., & Neri, R. 2002, A&A, 386, 633
Cox, P., Lucas, R., Huggins, P. J., et al. 2000, A&A, 353, L25
Dougados, C., Rouan, D., & Léna, P. 1992, A&A, 253, 464
Forveille, T., Morris, M., Omont, A., & Likkel, L. 1987, A&A, 176, L13
Geballe, T. R., Kim, Y. H., Knacke, R. F., & Keith, S. N. 1988, ApJ, 326, L65
Goodrich, R. W. 1991, ApJ, 376, 654
Guilloteau, S., Delannoy, J., Downes, D., et al. 1992, A&A, 262, 624
Klaus-Werner, H., Sellgren, K., & Nagata, T. 1988, ApJ, 326, L61
Langill, P. P., Kwok, S., & Hrivnak, B. J. 1994, PASP, 106, 736
Lopez, B., Tuthill, P. G., Danchi, W. C., Monnier, J. D., & Niccolini, G. 2001, A&A, 377, 90
Mauron, N., Le Borgne, J.-F., & Picquette, M. 1989, A&A, 218, 213
Morris, M. 1987, PASP, 99, 1115
Morris, M., & Reipurth, B. 1990, PASP, 102, 446
Omont, A., Moseley, S. H., Forveille, T., et al. 1990, ApJ, 355, L27
Phillips, J. P., & Cuesta, L. 1997, A&A, 326, 831
Robinson, G., Smith, R. G., & Hyland, A. R. 1992, MNRAS, 256, 437
Roddier, F., Roddier, C., Graves, J. E., & Northcott, M. J. 1995, ApJ, 443, 249
Rouan, D., Omont, A., Lacombe, F., & Forverille, T. 1988, A&A, 189, L3
Sahai, R., Bujarrabal, V., Castro-Carrizo, A., & Zijlstra, A. 2000, A&A, 360, L9
Sánchez Contreras, C., Bujarrabal, V., Castro-Carrizo, A., Alcolea, J., & Sargent, A. 2004, ApJ, in press
Scarrott, S. M., & Scarrott, R. M. J. 1994, MNRAS, 268, 615
Schönberner, D. 1983, ApJ, 272, 708
Van Dishoeck, E. F., & Black, J. H. 1998, ApJ, 334, 771

Online Material

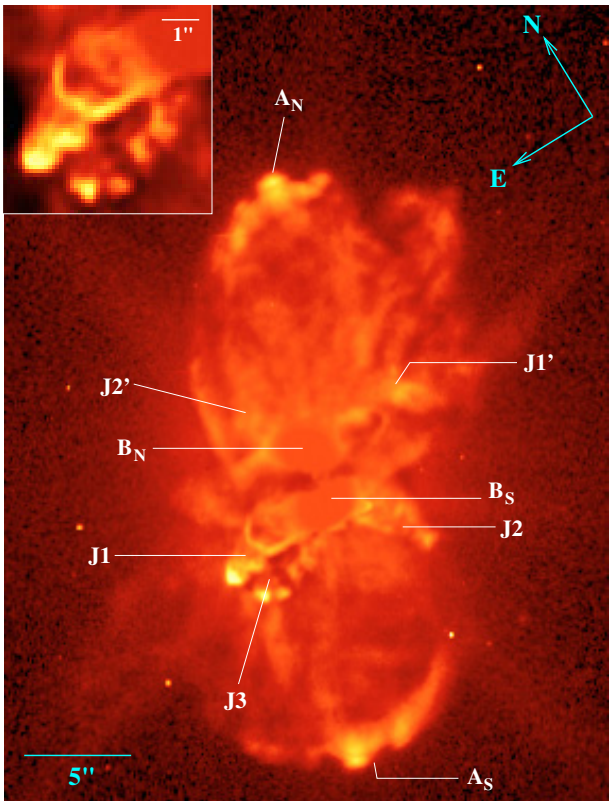

Fig. 1. Processed image from the original one at 0.6 μm observed by the Hubble Space Telescope (with the wide-band *F*606*W*/POLQ filter/polariser; see Sahai et al. 2000), which enphasizes the sharp features of Frosty Leo. Several jets (J1, J2, J3, J1′, J2′) are identified and labeled in the figure. Inset shows expanded view of jets J1 and J3. Northern and eastern directions are shown in right-upper corner. The PA of the (main) symmetry axis of this optical nebula is 150°.

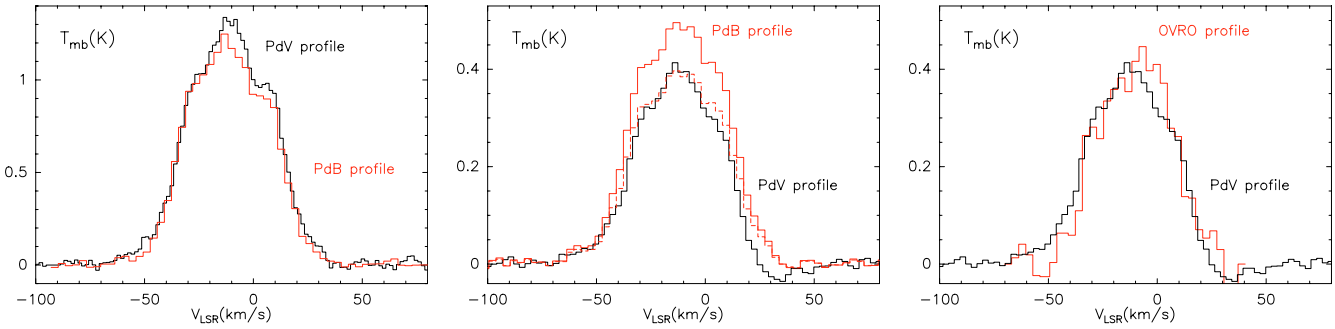

Fig. 5. Profiles of the emission coming from Frosty Leo for the rotational ^{12}CO transitions (*left*) $J = 2-1$, by the PdB interferometer, (*center*) $J = 1-0$, by the PdB array, and (*right*) 1–0, by the OVRO array. The PdV profiles are presented with a black line, and with a red line those of PdB or OVRO. With a dashed line the PdB $J = 1-0$ profile decreased by 20% is shown. In general, the fitting of the PdB and OVRO profiles with the PdV data is very satisfactory. In particular, the global intensity difference found for the transition $J = 1-0$ between the PdB and PdV data is probably caused by an inconsistence in the flux calibration used for both observatories. The shape of the OVRO profile fits less well that of PdV, due to noise limitation.

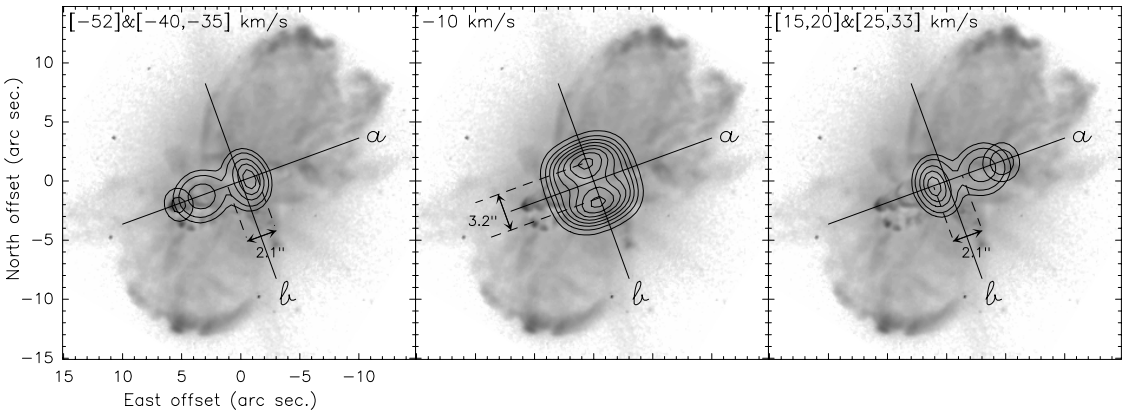

Fig. 9. In contours, the average of the intensity predicted by modeling the CO $J = 2-1$ emission, for the velocity ranges shown in the left-upper corner, over the optical image obtained by the HST. Contour levels, box sizes, velocity ranges and all labels are the same that in Fig. 6 to compare the most remarkable detected nebular components with those modeled.